

Universal Quantum Gate Set Approaching Fault-Tolerant Thresholds with Superconducting Qubits

Jerry M. Chow, Jay M. Gambetta, A.D. Córcoles, Seth T. Merkel, John A. Smolin, Chad Rigetti, S. Poletto, George A. Keefe, Mary B. Rothwell, J.R. Rozen, Mark B. Ketchen, and M. Steffen

IBM T.J. Watson Research Center, Yorktown Heights, New York 10598, USA

(Received 5 March 2012; published 9 August 2012)

We use quantum process tomography to characterize a full universal set of all-microwave gates on two superconducting single-frequency single-junction transmon qubits. All extracted gate fidelities, including those for Clifford group generators, single-qubit $\pi/4$ and $\pi/8$ rotations, and a two-qubit controlled-NOT, exceed 95% (98%), without (with) subtracting state preparation and measurement errors. Furthermore, we introduce a process map representation in the Pauli basis which is visually efficient and informative. This high-fidelity gate set serves as a critical building block towards scalable architectures of superconducting qubits for error correction schemes and pushes up on the known limits of quantum gate characterization.

DOI: [10.1103/PhysRevLett.109.060501](https://doi.org/10.1103/PhysRevLett.109.060501)

PACS numbers: 03.67.Ac, 03.67.Lx, 42.50.Pq, 85.25.-j

A critical prerequisite for building a scalable fault-tolerant quantum computer is the application of error correction codes [1–3]. In order to employ these codes, quantum gates must be performed with high fidelity above certain threshold levels. To build a practical quantum computer, it is not just important to further improve gate fidelities but also to fully characterize a universal gate set with a system-independent fidelity metric to compare different physical systems.

Two-dimensional error correction surface codes, with gate fidelity thresholds of ~ 90 – 99.5% depending on measurement errors [2–4], are amenable to implementation with superconducting circuits by using repetitive tiling of qubits and resonators into nearest-neighbor lattices [5]. Superconducting qubits have matured considerably as a candidate quantum computing system, with single-qubit gate fidelities now exceeding 99% [6,7], two-qubit gates generating entangled state fidelities greater than 90% [8–10], and three-qubit entanglement experiments [11]. Furthermore, recent results demonstrating tenfold increases in coherence times of Josephson-junction qubits [7,12,13] suggest that characterization of a complete high-fidelity universal set of quantum gates in superconducting qubits should be realizable.

In this Letter, we report gate fidelities greater than 95% for a complete universal set of gates for two fixed-frequency superconducting qubits. The qubits are single-junction transmons (SJTs), coupled via a coplanar waveguide resonator [14]. By using SJTs and modifying the qubit design, we increased the coherence times for our two SJTs to ~ 10 μ s. The gates characterized in this work include the single-qubit rotations $\{I, X_\pi, X_{\pi/2}, Y_{\pi/2}, X_{\pi/4}, X_{\pi/8}\}$ on both qubits (U_θ represents a rotation of angle θ around axis U) and a two-qubit controlled-NOT (CNOT) gate. The combination of the $\pi/4$ rotation (commonly referred to as the $\pi/8$ gate [15]), the Clifford group generators $\{X_{\pi/2}, Y_{\pi/2}\}$, and the two-qubit CNOT gate form a universal set [1]. The CNOT gate between the fixed-frequency qubits

is implemented using the cross-resonance (CR) interaction [9,16–18]. The gate fidelities are obtained via standard quantum process tomography (QPT) of each respective gate. Furthermore, here we also use a different but efficient visual representation of process maps, the Pauli transfer matrix \mathcal{R} . \mathcal{R} describes the action of a process on the components of the density matrix represented in the basis of Pauli operators and helps establish a number of properties of the underlying process which are otherwise hidden in the standard χ -matrix representation [15]. We find slight variations in the fidelities across the different gates and, from the associated maps, identify that our errors are not coherence limited but rather control limited and reflective of the sensitivity of QPT to state preparation and measurement errors. Randomized benchmarking of our single-qubit gates and a repeated CNOT experiment reveal that all of our gates have fidelities greater (98–99%) than those obtained by QPT. Our experiments, thus, also suggest that as superconducting qubits continue to improve in coherence times, both better controls and more efficient gate characterization schemes will become necessary.

The transmon qubit has become a popular choice for superconducting quantum computing applications due to its excellent coherence properties [14]. Implementations of transmons in planar qubit-cavity devices have traditionally been formed via capacitively shunting a Cooper-pair box, preserving tunability of the qubit transition frequencies. The ability to dynamically tune qubit frequencies is necessary for a number of entangling gate schemes [8,19] but often involves fast flux biasing to frequencies with reduced coherence. However, in this work we use only fixed-frequency SJTs, having previously implemented the all-microwave CR gate [9]. Importantly, here we further show that this CR gate is capable of high gate fidelities greater than 95% and permits a new paradigm for using only high-coherence fixed-frequency qubits, such as SJTs or 3D transmon qubits [7,13], for experiments with more qubits.

Two SJTs [Fig. 1(a)] with transition frequencies $\omega_1/2\pi = 5.0554$ GHz and $\omega_2/2\pi = 4.9895$ GHz are coupled via a 7.325 GHz coplanar waveguide resonator. Single-qubit rotations are performed by irradiating each qubit through independent on-chip microwave bias lines at the respective transition frequency. The relaxation times of the two qubits are measured to be $T_1^{(1)} = 8.2$ μ s and $T_1^{(2)} = 9.7$ μ s with Ramsey-fringe coherence times of $T_2^{(1)} = 7.1$ μ s and $T_2^{(2)} = 10.3$ μ s. We attribute the improved coherence times to reduced surface loss contributions [20] via larger qubit feature sizes [10 μ m capacitive shunt fingers and gaps; see Fig. 1(a)] and meticulous radiation shielding techniques [12,21]. Further sample details are given in the Supplemental Material [22].

We employ a series of repeated pulse experiments to accurately calibrate microwave amplitudes, offsets, and phases of single-qubit rotations [22]. The single-qubit rotations are shaped Gaussian envelopes (Gaussian width $\sigma = 10$ ns, total gate length 4σ) with derivative Gaussian quadrature corrections to account for excited state leakage [6,23].

The two-qubit interaction is the CR effect, and its implementation and advantages as a scalable multiqubit gate scheme are previously detailed in Refs. [9,17]. To review, the CR_{ij} effect is exhibited as a qubit i (control) state-dependent drive of qubit j (target). In our system, we drive microwaves resonant with qubit 2 onto the microwave bias line addressing qubit 1. A residual classical cross-talk term

is present, characterized by the parameter $m_{12} = 0.32$, which is the fraction of the direct Rabi frequency experienced by qubit 2 through driving on qubit 1. The strength of the desired two-qubit quantum effect is bounded by the residual qubit-qubit cavity-mediated dispersive interaction, found to be $J/\pi = 7.44$ MHz from detailed spectroscopy of transmon energy transitions and comparison to diagonalization of the Hamiltonian for our multilevel system. The detailed experimental tune-up and implementation of a CNOT gate with this interaction follows that of Ref. [9], and in this work the pulse shape is a flat-top Gaussian ($\sigma = 10$ ns) of length 110 ns.

To measure the two-qubit state, we employ a series of joint two-qubit measurements via nonlinear driving of the cavity [24]. Calibrating this joint measurement [22], we perform state tomography on arbitrary two-qubit states through the application of an overcomplete set of analysis pulses $\{I, X_\pi, X_{\pm\pi/2}, Y_{\pm\pi/2}\}^{\otimes 2}$ ($\otimes 2$ refers to all combinations over both qubits). An efficient maximum-likelihood estimation (MLE) algorithm [25] is used to compute two-qubit states which can be represented by the Pauli state vector \vec{p} [26]. The elements of \vec{p} are the expectation values of the two-qubit Pauli operators $\langle UV \rangle$, where $U, V \in I, X, Y, Z$ act on different qubits.

QPT is accomplished through the compilation of an overcomplete set of 36×36 measurements [Fig. 1(b)]. State tomography as described above is performed for the 36 different input states generated by $\{I, X_\pi, X_{\pm\pi/2}, Y_{\pm\pi/2}\}^{\otimes 2}$. Instead of the standard χ -matrix representation of the process map [15], we use a Pauli basis to represent the map, which we call the Pauli transfer matrix \mathcal{R} . \mathcal{R} maps an input Pauli state vector \vec{p}_{in} to an output Pauli state vector \vec{p}_{out} , $\vec{p}_{\text{out}} = \mathcal{R}\vec{p}_{\text{in}}$. \mathcal{R}_{raw} is the experimental map found by inversion of the raw data and \mathcal{R}_{mle} is the experimental map taking into account physical assumptions (complete positivity and trace preserving) found by an MLE algorithm that takes into account the covariance matrix for the different independent measurements [22]. The gate fidelity F_g is calculated from the \mathcal{R} map by $F_g = (\text{Tr}[\mathcal{R}_{\text{ideal}}^\dagger \mathcal{R}] + d)/(d^2 + d)$ with $d = 2n$, and n is the number of qubits with $\mathcal{R}_{\text{ideal}}$ being the ideal implementation of the map.

We perform QPT for the processes corresponding to the identity operation $I^{\otimes 2}$, all independent single-qubit rotations of π , $\pi/2$ (around x and y axes), $\pi/4$, and $\pi/8$, as well as the CNOT_{12} operation. The experimentally extracted map \mathcal{R}_{mle} for the single-qubit $\pi/4$ rotation for qubit 1 is shown in Fig. 2(a), and the ideal $\mathcal{R}_{\text{ideal}}$ is shown in Fig. 2(b). From \mathcal{R} , we estimate $F_g = 0.968(7)$. \mathcal{R}_{mle} for the two-qubit entangling CNOT_{12} gate is shown in Fig. 3(a), from which we estimate $F_g = 0.950(7)$ up to single-qubit rotations. Within this set, the highest entangled state fidelity $F_s = 0.983$ corresponds to the state $(|00\rangle + i|01\rangle - |10\rangle + i|11\rangle)/2$, with an associated concurrence $\mathcal{C} = 0.994$. The extracted F_g for the complete set of gates are given in Table I.

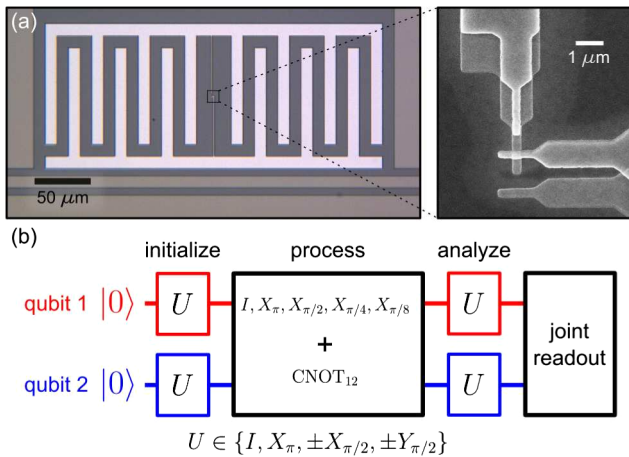


FIG. 1 (color online). Single-junction transmon and quantum process tomography pulse sequence. (a) Optical micrograph of a single-junction transmon device shown coupled to the center pin of a microwave resonator. The design is similar to standard transmon devices, with interdigitated capacitors shunting the Al/AIO_x Josephson junction on either side. Inset: scanning-electron micrograph of the Josephson junction with critical current $I_0 = 28$ nA. (b) Pulse sequence for performing quantum process tomography. An overcomplete set of rotations $\{I, X_\pi, X_{\pm\pi/2}, Y_{\pm\pi/2}\}$ is used to generate input states and to analyze the process before joint readout via the cavity.

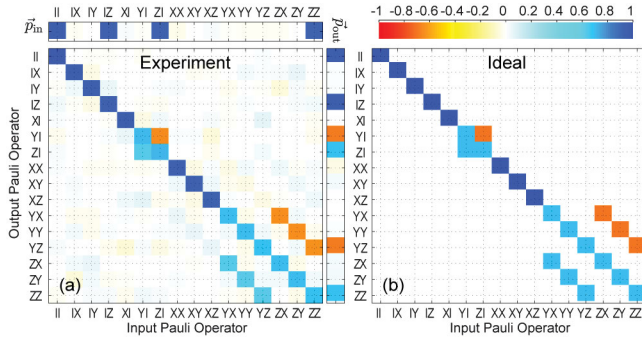


FIG. 2 (color). Quantum process tomography for $X_{\pi/4} \otimes I$ represented as the Pauli transfer matrix \mathcal{R} . (a) Experimentally extracted \mathcal{R}_{mle} for $X_{\pi/4} \otimes I$ with gate fidelity $F_g = 0.968(7)$. To illustrate the action of \mathcal{R}_{mle} , an input state $|00\rangle$ in the Pauli state vector form \vec{p}_{in} is shown above \mathcal{R}_{mle} , and the output state $\cos(\pi/8)|00\rangle - i\sin(\pi/8)|10\rangle$ ($F_s = 0.997$), represented as \vec{p}_{out} , is shown to the right. (b) Ideal $\mathcal{R}_{\text{ideal}}$ for $X_{\pi/4} \otimes I$.

Figures 2(a) and 3(a) also demonstrate the action of the different Pauli transfer maps on specific input states. Above the experimentally extracted \mathcal{R}_{mle} are the measured Pauli state vectors corresponding to $|00\rangle$ and $(|0\rangle + i|1\rangle) \times (|0\rangle + i|1\rangle)/2$ in Figs. 2(a) and 3(a), respectively. We can follow all the elements of each of these Pauli states downwards in the figures into \mathcal{R}_{mle} , which transfers these weights over into the Pauli operators to the right of \mathcal{R}_{mle} . Therefore, the Pauli state to the right reflects the output state given the operation of the map \mathcal{R}_{mle} on the input Pauli state vector, and this visualization very simply demonstrates its effect.

The \mathcal{R} representation is a more efficient and intuitive method for representing a quantum operation than the standard χ matrix [15], as it consists of only real numbers and possesses a few other nice visual properties. First, it is simple to tell if the map is trace preserving, which amounts to $\mathcal{R}_{II,jk} = \delta_{Ij}\delta_{Ik}$ for all $j, k \in \{I, X, Y, Z\}$. Next, we can also determine if the map is unital, if $\mathcal{R}_{jk,II} = \delta_{Ij}\delta_{Ik}$ for all $j, k \in \{I, X, Y, Z\}$. Finally, the elements in \mathcal{R} are bounded by ± 1 , and for any Clifford operation there is exactly one nonzero element in each row and column with unit magnitude.

It is possible to further investigate \mathcal{R} to understand the errors in our system and determine whether the loss in fidelity for the gates is statistical or systematic. For statistical errors, we use a parametric bootstrapping method which generates new realizations of tomography experiments based on the variance of our measurement operator calibrations [22]. From these generated experiments, new MLE ensembles are obtained and the variance of these ensembles serves as an upper bound on statistical fluctuations of our estimated gate errors [22]. For all of the gates studied in this work, the statistical component is found to be $\sim(4-7) \times 10^{-4}$ (Table I), much smaller than the QPT extracted gate errors of $\approx 5\%$.

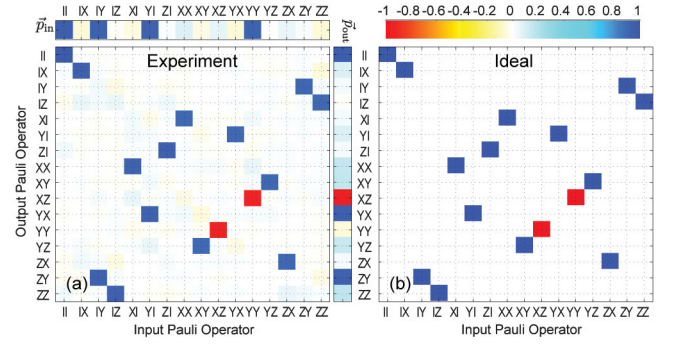


FIG. 3 (color). Quantum process tomography for the CNOT_{12} operation represented as the Pauli transfer matrix \mathcal{R} . (a) Experimentally extracted \mathcal{R}_{mle} for the CNOT_{12} operation with gate fidelity $F_g = 0.9507$. To illustrate the action of \mathcal{R}_{mle} , an input state $(|0\rangle + i|1\rangle)(|0\rangle + i|1\rangle)/2$ represented as \vec{p}_{in} is shown above \mathcal{R}_{mle} , and the output entangled state $(|00\rangle + i|01\rangle - |10\rangle + i|11\rangle)/2$ ($F_s = 0.9827$, $C = 0.994$), represented as \vec{p}_{out} , is shown to the right. (b) Ideal $\mathcal{R}_{\text{ideal}}$ for the CNOT_{12} operation.

The small value for statistical fluctuations suggests that our primary sources of error are systematic in nature. These can include decoherence, over- or under-rotations, and phase errors, all of which can occur during the actual processes to be characterized or during the state preparation and measurement analysis gates. Given the coherence and gate times of the QPT sequence, we estimate a total error of 1.62% for single-qubit gates and 2.55% for the CNOT gate, which is still smaller than the observed error and not the primary source.

The remaining error can be attributed to 1% miscalibration in the single-qubit gates used for preparation and analysis. Simulations of \mathcal{R} including this level of calibration error agree well with the nonideal elements found in $\mathcal{R}_{\text{ideal}}$ [22]. This is further confirmed through

TABLE I. Summary of gate fidelity F_g obtained from \mathcal{R}_{raw} , obtained from the MLE processed \mathcal{R}_{mle} , statistical error ΔF_g , purified fidelity F_{pure} , and nonphysical error $Y_{\text{np}} = 0.5\|\mathcal{R}_{\text{raw}} - \mathcal{R}_{\text{mle}}\|_2$ for a complete universal set of gates on two qubits.

Gate	F_g (raw)	F_g (mle)	$\Delta F_g (\times 10^{-4})$	F_{pure}	Y_{np}
$I \otimes I$	0.9780	0.9691	3.6	0.9954	0.036
$X_{\pi} \otimes I$	0.9707	0.9618	4.3	0.9935	0.029
$X_{\pi/2} \otimes I$	0.9709	0.9620	5.2	0.9955	0.030
$Y_{\pi/2} \otimes I$	0.9744	0.9621	5.3	0.9956	0.046
$X_{\pi/4} \otimes I$	0.9777	0.9687	5.5	0.9962	0.038
$X_{\pi/8} \otimes I$	0.9744	0.9649	5.2	0.9962	0.038
$I \otimes X_{\pi}$	0.9725	0.9629	4.4	0.9906	0.033
$I \otimes X_{\pi/2}$	0.9692	0.9597	3.9	0.9955	0.031
$I \otimes Y_{\pi/2}$	0.9743	0.9569	4.6	0.9961	0.040
$I \otimes X_{\pi/4}$	0.9763	0.9644	4.6	0.9963	0.035
$I \otimes X_{\pi/8}$	0.9757	0.9666	6.0	0.9968	0.042
CNOT_{12}	0.9675	0.9507	6.5	0.9968	0.035

TABLE II. The error budget.

Mechanism	Error
Statistical errors (ΔF_g)	0.1%
T_1/T_2 (simulation from $1 - F_g$)	1.5–2.6%
Unitary error in gate ($1 - F_{\text{pure}}$)	0.5–1%
Nonphysical errors (Y_{np})	3%
Total ($1 - F_g$)	3.5–5%

the calculation of the purified fidelity, F_{pure} , which estimates how close the unitary contribution of the map is to the ideal gate. F_{pure} is defined as the overlap of the ideal map with the maximum eigenvector of the Choi matrix [27] corresponding to \mathcal{R}_{mle} [22]. For all of the gates investigated, $F_{\text{pure}} > 0.99$ (Table I), indicating that we perform the correct unitary to better than $\approx 1\%$, but we are adding on nonpurity conserving operations due to systematic errors. These errors can be quantified via $Y_{\text{np}} = 0.5\|\mathcal{R}_{\text{raw}} - \mathcal{R}_{\text{mle}}\|_2$, which is half the two-norm distance between the raw experimental \mathcal{R}_{raw} and the most likely physical map \mathcal{R}_{mle} . For all gates, $Y_{\text{np}} \approx 3\text{--}4\%$ (Table I), which suggests that propagation of small errors in our preparation and measurement operations in the QPT accounts for a large portion of the gate errors obtained experimentally [22].

Table II summarizes the different mechanisms to which we attribute our gate error budget. More discussion regarding these error metrics is given in the SM [22]. Our QPT analysis further reinforces the importance of other methods for gate characterization, such as randomized benchmarking (RB) [28], as F_g can be significantly misrepresented due to small systematic errors in preparation and analysis. For the single-qubit gates, using RB techniques we find much smaller gate errors of $\sim 0.2\text{--}0.3\%$ (details given in separate manuscripts [29]).

Finally, as a precursor to full two-qubit RB we show \mathcal{C} and F_s after the repeated application of CNOT gates on the input state generated by $X_{-\pi/2} \otimes I$. Figure 4(a) reveals \mathcal{C} for up to 12 applications of the CNOT operation, indicating as desired no entanglement for even numbers (N) of gates. In Fig. 4(b), we plot the F_s of the final state to the ideal states, the Bell state $(|00\rangle + i|11\rangle)/\sqrt{2}$ for odd N , and the input state $(|00\rangle + i|10\rangle)/\sqrt{2}$ for even N . By assuming an exponential model for the state fidelity, $F_s = AF_g^N + B$, with A and B as fit parameters (dashed black line), we extract gate fidelity $F_g = 0.984$. We find that this is in good agreement with a simulation of F_g taking into account the coherence parameters of the system and the durations of the gates involved in the experiment (solid blue line).

Thus, we have shown a complete universal set of high-fidelity gates on two high-coherence fixed-frequency superconducting qubits. Although the gate fidelities obtained via QPT are at the 95% level, both the analysis of the \mathcal{R} maps with only 1% systematic calibration errors and

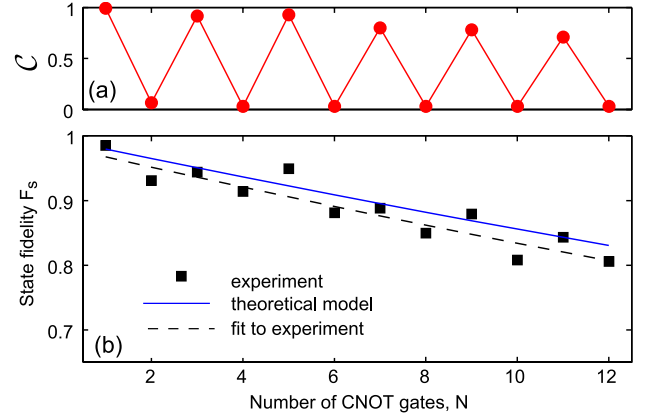


FIG. 4 (color online). Concurrence and state fidelity after N applications of the CNOT operation. (a) Concurrence \mathcal{C} of final states after applying N CNOT gates to input state $(|00\rangle + i|10\rangle)/\sqrt{2}$. (b) Black squares are the final state fidelity F_s of experimentally obtained states to the ideal Bell (original input) state for odd (even) N . The dashed black line is a fit to the data assuming a model of $AF_g^N + B$, where A , B , and gate fidelity F_g are fit parameters. The fit gives an error per gate $1 - F_g = 0.0164$. The solid blue line is a theoretical model using the measured coherence values and gate times.

the repeated CNOT sequences suggest that the intrinsic gate fidelities are $>98\%$, near the coherence time limit. Moving forward, finer pulse calibration tune-up sequences must be implemented, and gate errors will be characterized via RB to avoid systematic errors in state preparation and analysis. Nonetheless, this demonstration further paves the road towards multiqubit experiments for implementing more complicated pieces of quantum error correction.

We acknowledge experimental contributions from J. Rohrs, B.R. Johnson, T. Ohki, J. Strand, and B.L.T. Plourde. We acknowledge support from IARPA under Contract No. W911NF-10-1-0324.

- [1] P. Shor, in *37th Symposium on Foundations of Computing* (IEEE Computer Society Press, New York, 1996), p. 56; A. Steane, *Proc. R. Soc. A* **452**, 2551 (1996).
- [2] S. Bravyi and A. Kitaev, [arXiv:quant-ph/9811052](https://arxiv.org/abs/quant-ph/9811052); R. Raussendorf and J. Harrington, *Phys. Rev. Lett.* **98**, 190504 (2007).
- [3] A. W. Cross, D. P. Divincenzo, and B. M. Terhal, *Quantum Inf. Comput.* **9**, 541 (2009).
- [4] E. Dennis, A. Kitaev, A. Landahl, and J. Preskill, *J. Math. Phys. (N.Y.)* **43**, 4452 (2002).
- [5] M. Steffen, D. P. DiVincenzo, J. M. Chow, T. N. Theis, and M. B. Ketchen, *IBM J. Res. Dev.* **55**, 13:1 (2011).
- [6] J. M. Chow, L. DiCarlo, J. M. Gambetta, F. Motzoi, L. Frunzio, S. M. Girvin, and R. J. Schoelkopf, *Phys. Rev. A* **82**, 040305 (2010).
- [7] H. Paik, D. I. Schuster, L. S. Bishop, G. Kirchmair, G. Catelani, A. P. Sears, B. R. Johnson, M. J. Reagor, L.

- Frunzio, L. I. Glazman, S. M. Girvin, M. H. Devoret, and R. J. Schoelkopf, *Phys. Rev. Lett.* **107**, 240501 (2011).
- [8] L. DiCarlo, J. M. Chow, J. M. Gambetta, L. S. Bishop, B. R. Johnson, D. I. Schuster, J. Majer, A. Blais, L. Frunzio, S. M. Girvin, and R. J. Schoelkopf, *Nature (London)* **460**, 240 (2009).
- [9] J. M. Chow, A. D. Corcoles, J. M. Gambetta, C. Rigetti, B. R. Johnson, J. A. Smolin, J. R. Rozen, G. A. Keefe, M. B. Rothwell, M. B. Ketchen, and M. Steffen, *Phys. Rev. Lett.* **107**, 080502 (2011).
- [10] A. Dewes, F. R. Ong, V. Schmitt, R. Lauro, N. Boulant, P. Bertet, D. Vion, and D. Esteve, *Phys. Rev. Lett.* **108**, 057002 (2012).
- [11] L. DiCarlo, M. D. Reed, L. Sun, B. R. Johnson, J. M. Chow, J. M. Gambetta, L. Frunzio, S. M. Girvin, M. H. Devoret, and R. J. Schoelkopf, *Nature (London)* **467**, 574 (2010); M. Neeley, R. C. Bialczak, M. Lenander, E. Lucero, M. Mariantoni, A. D. O'Connell, D. Sank, H. Wang, M. Weides, J. Wenner, Y. Yin, T. Yamamoto, A. N. Cleland, and J. M. Martinis, *ibid.* **467**, 570 (2010).
- [12] A. D. Corcoles, J. M. Chow, J. M. Gambetta, C. Rigetti, J. R. Rozen, G. A. Keefe, M. Beth Rothwell, M. B. Ketchen, and M. Steffen, *Appl. Phys. Lett.* **99**, 181906 (2011).
- [13] C. Rigetti, S. Poletto, J. M. Gambetta, B. Plourde, J. M. Chow, A. Corcoles, S. T. Merkel, J. A. Smolin, J. R. Rozen, G. A. Keefe, M. B. Rothwell, M. B. Ketchen, and M. Steffen, [arXiv:1202.5533v1](https://arxiv.org/abs/1202.5533v1).
- [14] J. Koch, T. M. Yu, J. Gambetta, A. A. Houck, D. I. Schuster, J. Majer, A. Blais, M. H. Devoret, S. M. Girvin, and R. J. Schoelkopf, *Phys. Rev. A* **76**, 042319 (2007); J. A. Schreier, A. A. Houck, J. Koch, D. I. Schuster, B. R. Johnson, J. M. Chow, J. M. Gambetta, J. Majer, L. Frunzio, M. H. Devoret, S. M. Girvin, and R. J. Schoelkopf, *Phys. Rev. B* **77**, 180502(R) (2008).
- [15] M. A. Nielsen and I. L. Chuang, *Quantum Computation and Quantum Information* (Cambridge University Press, Cambridge, England, 2000).
- [16] G. S. Paraoanu, *Phys. Rev. B* **74**, 140504 (2006).
- [17] C. Rigetti and M. Devoret, *Phys. Rev. B* **81**, 134507 (2010).
- [18] P. C. de Groot, S. Ashhab, A. Lupascu, L. DiCarlo, F. Nori, C. J. P. M. Harmans, and J. E. Mooij, [arXiv:1201.3360](https://arxiv.org/abs/1201.3360).
- [19] M. Ansmann, H. Wang, R. C. Bialczak, M. Hofheinz, E. Lucero, M. Neeley, A. D. O'Connell, D. Sank, M. Weides, J. Wenner, A. N. Cleland, and J. M. Martinis, *Nature (London)* **461**, 504 (2009).
- [20] J. Wenner, R. Barends, R. C. Bialczak, Y. Chen, J. Kelly, E. Lucero, M. Mariantoni, A. Megrant, P. J. J. O'Malley, D. Sank, A. Vainsencher, H. Wang, T. C. White, Y. Yin, J. Zhao, A. N. Cleland, and J. M. Martinis, *Appl. Phys. Lett.* **99**, 113513 (2011).
- [21] R. Barends, J. Wenner, M. Lenander, Y. Chen, R. C. Bialczak, J. Kelly, E. Lucero, P. O'Malley, M. Mariantoni, D. Sank, H. Wang, T. C. White, Y. Yin, J. Zhao, A. N. Cleland, J. M. Martinis, and J. J. A. Baselmans, *Appl. Phys. Lett.* **99**, 113507 (2011).
- [22] See Supplemental Material at <http://link.aps.org/supplemental/10.1103/PhysRevLett.109.060501> for details on the sample, calibration techniques, Pauli transfer map representation, and error estimates.
- [23] F. Motzoi, J. M. Gambetta, P. Rebentrost, and F. K. Wilhelm, *Phys. Rev. Lett.* **103**, 110501 (2009).
- [24] M. D. Reed, L. DiCarlo, B. R. Johnson, L. Sun, D. I. Schuster, L. Frunzio, and R. J. Schoelkopf, *Phys. Rev. Lett.* **105**, 173601 (2010).
- [25] J. A. Smolin, J. M. Gambetta, and G. Smith, *Phys. Rev. Lett.* **108**, 070502 (2012).
- [26] J. M. Chow, L. DiCarlo, J. M. Gambetta, A. Nunnenkamp, L. S. Bishop, L. Frunzio, M. H. Devoret, S. M. Girvin, and R. J. Schoelkopf, *Phys. Rev. A* **81**, 062325 (2010).
- [27] M.-D. Choi, *Linear Algebra Appl.* **10**, 285 (1975).
- [28] E. Magesan, J. M. Gambetta, and J. Emerson, *Phys. Rev. Lett.* **106**, 180504 (2011).
- [29] E. Magesan, J. M. Gambetta, B. R. Johnson, C. A. Ryan, J. M. Chow, S. T. Merkel, M. P. da Silva, G. A. Keefe, M. B. Rothwell, T. A. Ohki, M. B. Ketchen, and M. Steffen, [arXiv:1203.4550v1](https://arxiv.org/abs/1203.4550v1); J. M. Gambetta, A. D. Corcoles, S. T. Merkel, B. R. Johnson, J. A. Smolin, J. M. Chow, C. A. Ryan, C. Rigetti, S. Poletto, T. A. Ohki, M. B. Ketchen, and M. Steffen, [arXiv:1204.6308v1](https://arxiv.org/abs/1204.6308v1).